Chemical Science

EDGE ARTICLE

View Article Online
View Journal | View Issue



Cite this: *Chem. Sci.*, 2024, **15**, 19546

All publication charges for this article have been paid for by the Royal Society of Chemistry

# Strain-induced charge delocalization achieves ultralow exciton binding energy toward efficient photocatalysis†

Junyuan Duan,‡[ab] Yinghe Zhao,‡[a] Yu Wu,[a] Youwen Liu,*[a] Junnian Chen,[e] Ruoou Yang,[a] Jiazhao Huang,[a] Chuanqi Luo,[a] Mao Wu,[a] Xiaodong Zheng,[d] Pengyu Li,[a] Xueliang Jiang,*[b] Jianguo Guan*[c] and Tianyou Zhai[a]

The exciton effect is commonly observed in photocatalysts, where substantial exciton binding energy ($E_b$) significantly hampers the efficient generation of photo-excited electron–hole pairs, thereby severely constraining photocatalysis. Herein, we propose a strategy to reduce $E_b$ through strain-induced charge delocalization. Taking $Ta_2O_5$ as a prototype, tensile strain was introduced by engineering a crystalline/amorphous interface, weakening the interaction between Ta 5d and O 2p orbitals, thus endowing a delocalized charge transport and significantly lowering $E_b$. Consequently, the $E_b$ of strained $Ta_2O_5$ nanorods (s-$Ta_2O_5$ NRs) was reduced to 24.26 meV, below the ambient thermal energy (26 meV). The ultralow $E_b$ significantly enhanced the yield of free charges, resulting in a two-fold increase in carrier lifetime and surface potential. Remarkably, the hydrogen evolution rate of s-$Ta_2O_5$ NRs increased 51.5 times compared to that of commercial $Ta_2O_5$. This strategy of strain-induced charge delocalization to significantly reduce $E_b$ offers a promising avenue for developing advanced semiconductor photoconversion systems.

Received 1st September 2024
Accepted 3rd November 2024

DOI: 10.1039/d4sc05873a

rsc.li/chemical-science



## Introduction

Photocatalysis has emerged as a promising approach to tackle energy and environmental challenges by harnessing solar energy for conversion into chemical energy,[1–6] exemplified by the production of hydrogen through photocatalytic water splitting.[7,8] When a semiconductor catalyst absorbs photons with energy exceeding its bandgap energy ($E_g$), it excites electrons from the valence band (VB) to the conduction band (CB), while simultaneously generating positive holes in the VB (process I depicted in Fig. 1a).[1,3,9] Furthermore, the coulombic attraction between these electrons and holes can give rise to the formation of bound state excitons (process II depicted in Fig. 1a),[10–13] known as the exciton effect, which is frequently overlooked. Given the neutral nature of excitons,[14,15] their direct involvement in photocatalytic reactions is precluded; hence, it becomes imperative to mitigate the exciton effect for augmenting the abundance of free charges and thereby enhancing photocatalytic efficiency.[16–18] According to the Saha–Langmuir equation $\frac{x^2}{1-x} = \frac{1}{n}\left(\frac{2\pi\mu k_B T}{h^2}\right)^{3/2} e^{-E_b/k_B}$ (where $x$, $n$, $\mu$, $T$ and $h$ represent the free charge fraction, number of energetic particles, reduced mass of the exciton, temperature and Planck constant respectively),[19] the exciton binding energy ($E_b$), a key parameter for evaluating the strength of the exciton effect, determines the ratio of free charges to excitons at a certain temperature and excitation density.

Ambient thermal energy ($k_BT \approx 26$ meV, where $k_B$ is the Boltzmann constant and $T$ is temperature) serves as a critical benchmark for evaluating exciton stability.[20] Excitons with $E_b$ above this threshold exhibit greater stability and resistance to dissociation into free charges, whereas those with lower $E_b$ are more susceptible to dissociation. To promote efficient exciton dissociation, researchers exert considerable efforts,[9,21–25] such as typically employing charge spatial separation within heterojunctions, creating an internal electric field that reduces $E_b$ and boosts free carrier generation.[16,18,26–31] However, due to the

[a]State Key Laboratory of Materials Processing and Die & Mould Technology, and School of Materials Science and Engineering, Huazhong University of Science and Technology, Wuhan, 430074, China. E-mail: ywliu@hust.edu.cn

[b]Hubei Key Laboratory of Plasma Chemistry and New Materials, School of Materials Science and Engineering, Key Laboratory of Green Chemical Engineering Process of Ministry of Education, Engineering Research Center of Phosphorus Resources Development and Utilization of Ministry of Education, Wuhan Institute of Technology, Wuhan, 430205, China. E-mail: jiangxl@wit.edu.cn

[c]State Key Laboratory of Advanced Technology for Materials Synthesis and Processing, Wuhan University of Technology, Wuhan, 430070, China. E-mail: guanjg@whut.edu.cn

[d]Department of Applied Physics, The Hong Kong Polytechnic University, Kowloon, Hong Kong, China

[e]School of Materials Science & Engineering, Hubei University, Wuhan, 430062, China

† Electronic supplementary information (ESI) available. See DOI: https://doi.org/10.1039/d4sc05873a

‡ These authors contributed equally to this work.

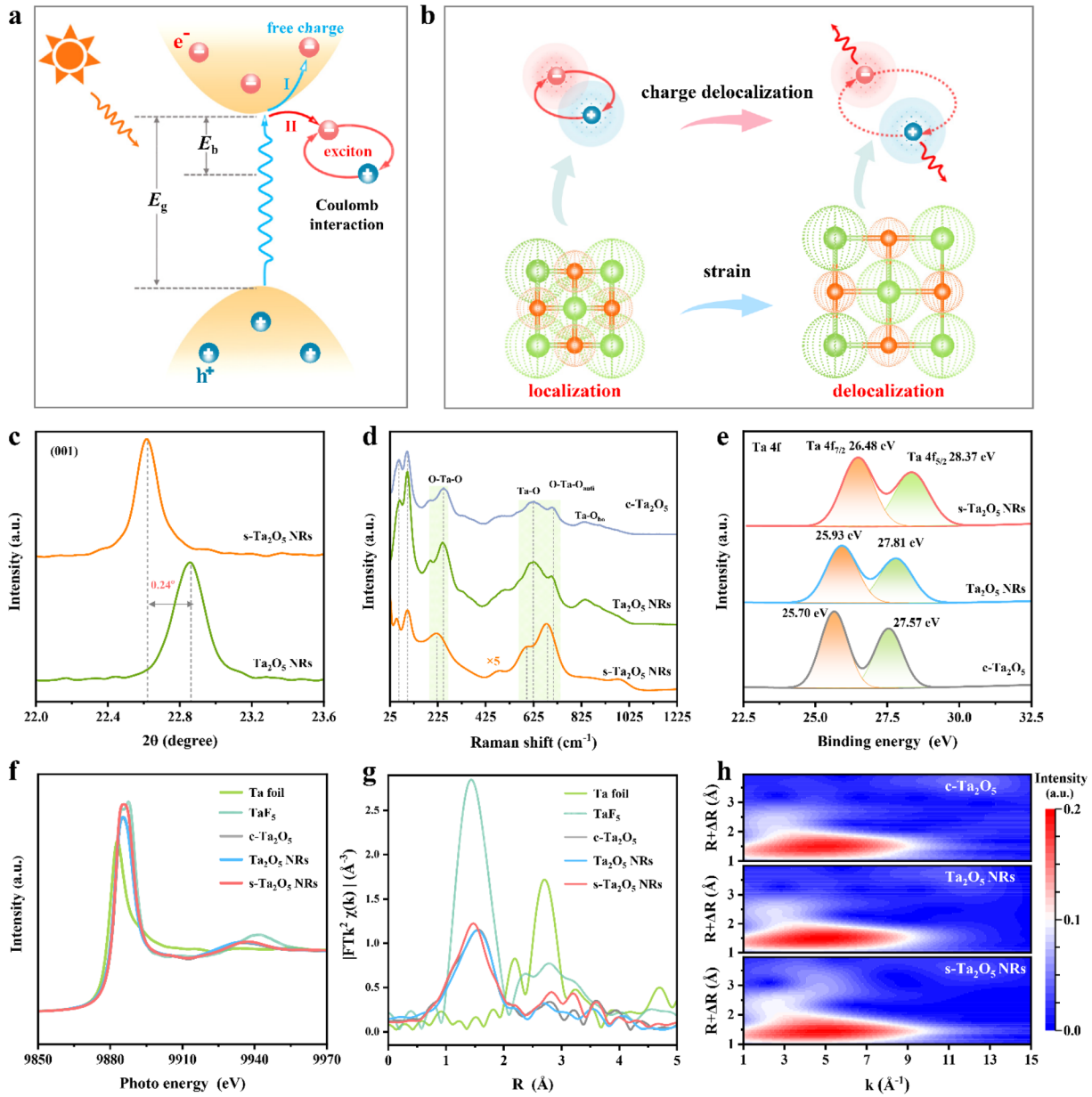


Fig. 1 Design scheme and structural characterization of s-$Ta_2O_5$ NRs. (a) Schematic of typical charge migration and the exciton effect in photocatalysis. (b) Strain-induced charge delocalization endows a delocalized charge transport pathway, minimizing the charge overlap between the electron and hole of the exciton and thus reducing $E_b$. (c) XRD patterns with an enlarged view of the (001) peak. (d) Raman spectra. (e) Ta 4f orbital XPS spectra. (f) Ta L3-edge XANES spectra. (g) $k^2$-weighted Fourier transform of the EXAFS spectra. (h) Wavelet transform of the $k^2$-weighted EXAFS.

significant charge localization inherent in the typical semiconductor catalyst lattice, which often leads to a strong interaction between the electron and hole in the resulting exciton, there are challenges in reducing the $E_b$ below ambient thermal energy. Therefore, developing new strategies to reduce the $E_b$ holds promise for achieving breakthroughs in photocatalytic performance.

Herein, by applying tensile strain to finely adjust charge localization and establish a delocalized transport pathway, we effectively reduce the $E_b$ without relying on external fields or interfaces (Fig. 1b). Taking $Ta_2O_5$ as a prototype with exceptional water splitting capability,[32–34] we achieved charge delocalization by constructing a tensile strain in $Ta_2O_5$ nanorods (s-$Ta_2O_5$ NRs). Density functional theory (DFT) calculations further validate that this strain weakens the interaction between Ta 5d and O 2p orbitals, fostering a more delocalized charge transfer channel and significantly increasing the dielectric constant ($\varepsilon_r$), thereby achieving a reduced $E_b$. A tensile strain markedly reduces the $E_b$ of s-$Ta_2O_5$ NRs to ~24.26 meV, below the thermal energy at room temperature ($k_BT$, 26 meV), achieving a reduction of 71.50% in comparison to $Ta_2O_5$ NRs. This reduction in $E_b$ doubles the carrier lifetime and surface

potential, enhancing the separation of photogenerated charges, increasing the yield and separation rate of free charges, and lowering the hydrogen evolution reaction barrier. Consequently, this facilitates direct electron transfer from Ta atoms to protons, markedly boosting photocatalytic hydrogen production, which is 51.5 times higher than that of c-$Ta_2O_5$. This study demonstrates that by reducing the exciton binding energy through tensile strain, we can optimize charge transfer and promote photogenerated charge-driven photocatalytic reactions, offering a new avenue for the design and preparation of efficient semiconductor photocatalytic materials.

## Results and discussion

### Structural characterization of s-$Ta_2O_5$ NRs

Herein, the s-$Ta_2O_5$ NRs with a tensile strain were successfully fabricated by ingeniously engineering a crystalline/amorphous interface within them, achieved through the strategic insertion of F atoms into the spaces between the vertices of $TaO_6$ octahedra and $TaO_7$ polyhedra. X-ray diffraction (XRD) analysis, as depicted in Fig. 1c and S1,† clearly demonstrates that these s-$Ta_2O_5$ NRs (Fig. S2†) exhibit the characteristic orthorhombic $Ta_2O_5$, with an evident tensile strain along the [001] axis and an amorphous nature in their orthogonal directions. This was further supported by Raman spectra, which not only confirmed the orthorhombic $Ta_2O_5$ phase but also evidenced the presence of tensile strain and a level of crystalline integrity reduction in the s-$Ta_2O_5$ NRs (Fig. 1d and Note S1 in the ESI†). Furthermore, X-ray photoelectron spectra (XPS) revealed an increase in the binding energies of the Ta 4f5/2 (28.37 eV) and Ta 4f7/2 orbitals (26.37 eV) in s-$Ta_2O_5$ NRs, suggesting an oxidation state beyond the typical +5 state,[35] attributed to the F atoms' integration into the matrix (Fig. S3a and c†). Energy-dispersive X-ray spectroscopy (EDS) mapping (Fig. S4†) revealed a uniform distribution of Ta, O, and F elements throughout the nanorods, with a relatively weaker signal for F, indicating its minor presence. XPS quantified the atomic proportions (Fig. S3†) as 20.99% Ta, 52.7% O, and 11.85% F, demonstrating that the s-$Ta_2O_5$ NRs not only contain the typical Ta–O bonds but also Ta–F bonds, suggesting a unique interstitial incorporation of F within the lattice, rather than simple substitutional doping. O 1s XPS and electron spin resonance (ESR) measurements (Fig. S3b and S5†) further confirmed the widespread occurrence of oxygen defects.

To further elucidate the structural coordination of Ta atoms within s-$Ta_2O_5$ NRs, the synchrotron radiation X-ray absorption fine structure (XAFS) spectra were recorded, and compared with those of $Ta_2O_5$ NRs (Fig. S6†) and c-$Ta_2O_5$ (Fig. S7†). Notably, the X-ray absorption near edge structure (XANES) spectra at the Ta L3 edge show that the s-$Ta_2O_5$ NRs display an absorption edge closely aligned with that of the other $Ta_2O_5$ samples but with a pronounced white line peak (Fig. 1f), suggesting a slightly higher oxidation state of Ta, potentially beyond +5, consistent with that by Ta 4f XPS spectra. Further, Fourier transform analysis of the extended X-ray absorption fine structure (EXAFS) reveals a dominant peak at approximately 1.48 Å for s-$Ta_2O_5$ NRs, indicating a shorter bond length compared to the 1.56 Å Ta–O bond in $Ta_2O_5$ NRs and c-$Ta_2O_5$, yet longer than the typical Ta–F bond of approximately 1.44 Å, attributed to the presence of Ta–F alongside Ta–O bonds (Fig. 1g). Additionally, this bond length is slightly longer than that observed in typical $Ta_2O_5$ samples, yet significantly shorter than the Ta–F bond, indicating a slight increase in coordination number and the incorporation of some fluorine into the s-$Ta_2O_5$ NRs lattice (Fig. 1g and S8†). Wavelet transform analysis further distinguishes the s-$Ta_2O_5$ NRs by showing similar Ta–O coordination within a 1–3 Å range to other samples, but with enhanced contours at 3–4 Å, indicative of a more distinct separation of Ta atoms, suggesting a degree of disordered structure induced by fluorine incorporation (Fig. 1h). According to the above XAFS results, the insertion of F atoms is inferred to have induced a significant degree of disordered structure within the s-$Ta_2O_5$ NRs lattice.

To examine the internal structure and strain of s-$Ta_2O_5$ NRs, high-resolution transmission electron microscopy (HRTEM) was performed. The HRTEM image of an individual s-$Ta_2O_5$ nanorod (Fig. 2a) clearly shows that it preferentially grows along the [001] axis, with an observed interplanar spacing of the (001) planes slightly increased to about 0.393 nm (Fig. S9†), a subtle yet notable expansion from the 0.388 nm spacing characteristic of the normal $Ta_2O_5$ crystal (PDF# 25-0922). Corresponding geometric phase analysis (GPA) further corroborates the presence of a uniform tensile strain of approximately 1.5% along this [001] axis (Fig. 2b). Only a set of bright diffraction spots manifested in the selected area electron diffraction (SAED) pattern (Fig. 2c), which affirms the single-crystal nature of the s-$Ta_2O_5$ NRs. Nevertheless, the occurrence of the 'tail-dragging' effect in the diffraction signals perpendicular to the [001] direction points to a significant structural disorder in the orthogonal plane. This is evidenced by high-resolution aberration-corrected high-angle annular dark-field (HAADF) scanning TEM images (STEM, Fig. 2d and e), which reveal a multitude of layer faults, including extra and missing atomic layers in the direction orthogonal to the [001]. Further HRTEM investigations (Fig. S10†) on additional s-$Ta_2O_5$ nanorods consistently demonstrate the aforementioned tensile strain along the [001] axis and a pronounced disordered structure in the orthogonal plane, consistent with the XRD and Raman spectra analyses.

To explore the atomic arrangement within the (001) plane of these special structured s-$Ta_2O_5$ NRs, focused ion beam (FIB) slices were made and then observed by aberration-corrected transmission electron microscopy. The resultant high-resolution HAADF-STEM image taken on the cross-section of an individual s-$Ta_2O_5$ nanorod (Fig. 2f and S11a†) clearly delineates a juxtaposition of both ordered and disordered atomic arrangement, alongside a multitude of discernible cavities. A closer inspection of the region labelled as 'g' in Fig. 2f clearly exhibits a highly ordered orthorhombic phase $Ta_2O_5$ atomic arrangement (Fig. 2g, S11b and S12†), with a slightly larger spacing between (200) planes (~0.317 nm) compared to the normal $Ta_2O_5$ crystal ($d(200) \approx 0.31$ nm). The corresponding GPA strain tensor mapping (Fig. 2h) further confirms the presence of a tensile strain of approximately 2% in the [200] direction. In stark contrast, the examination of region 'i' in

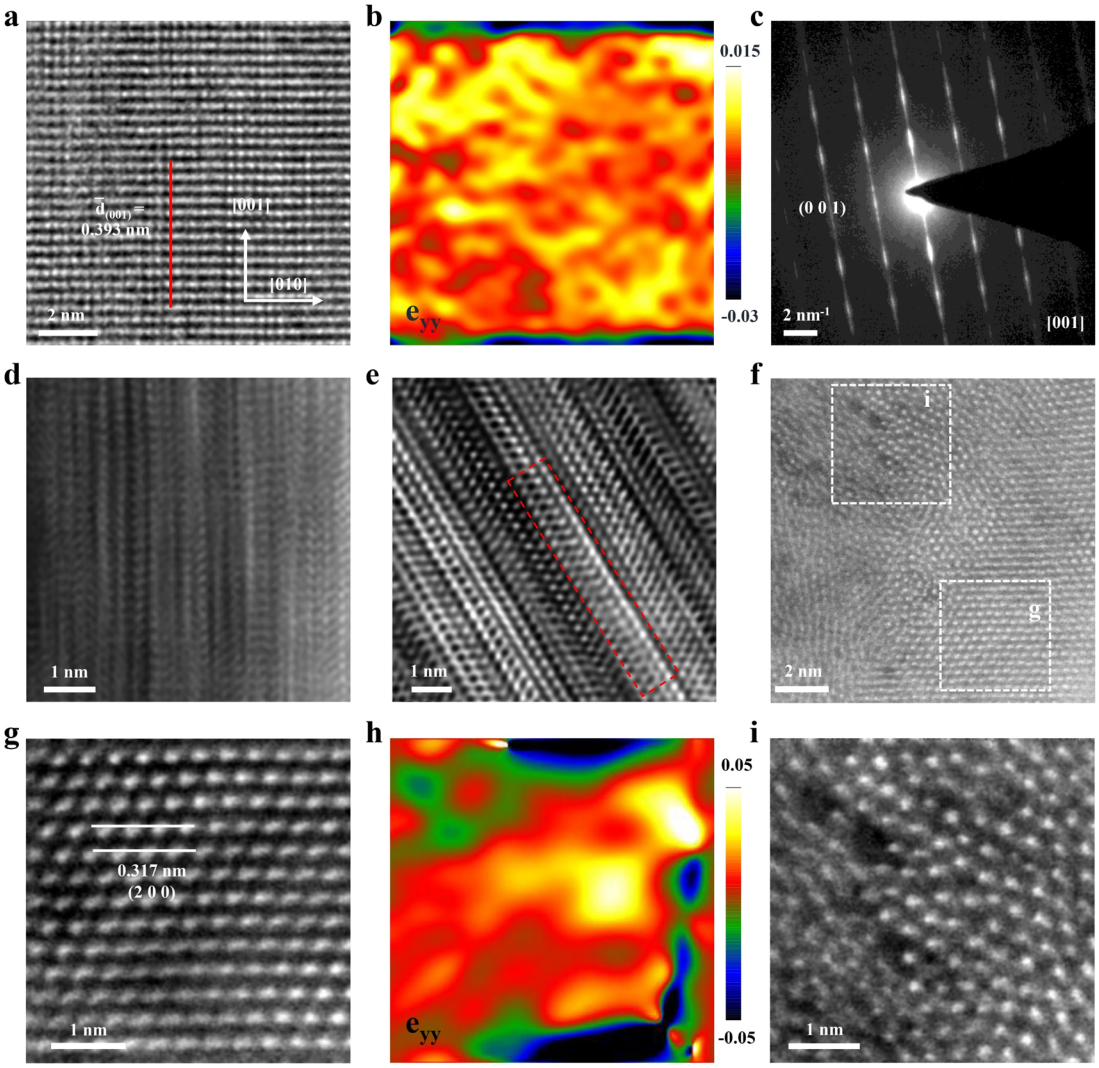


Fig. 2 Structural characterization of s-$Ta_2O_5$ NRs. (a) HRTEM image of the surface. (b) Corresponding $e_{yy}$ strain tensor derived from (a). (c) SAED pattern on the surface. (d) and (e) Aberration-corrected HAADF-STEM images of the surface. (f) Aberration-corrected HAADF-STEM image of the cross-section. (g) and (i) Enlarged views of the areas g and i marked by rectangles in (f), respectively. (h) Corresponding $e_{yy}$ strain tensor of (g).

Fig. 2f through an enlarged HAADF-STEM image (Fig. 2i) displays a starkly disordered atomic arrangement, replete with many noticeable cavities, indicative of an amorphous structure. More HAADF-STEM images (Fig. S13†) randomly sampled from the cross-section of another s-$Ta_2O_5$ nanorod evidence the repetitive nature of this intricate structural motif, comprising both crystalline and amorphous domains, as well as the consistent occurrence of tensile strain and cavities. Collectively, these observations substantiate that the s-$Ta_2O_5$ NRs possess a distinct single-crystal growth pattern along the [001] axis, seamlessly incorporating a blend of ordered and amorphous structures in the perpendicular orientation, and are characterized by the tensile strain within the crystalline regions of $Ta_2O_5$, alongside the pervasive presence of cavities.

Ultraviolet absorption and valence band spectra (Fig. S14†) have established s-$Ta_2O_5$ NRs as a prototypical semiconductor, with a similar band structure to both $Ta_2O_5$ NRs and c-$Ta_2O_5$ samples. It manifests a bandgap ($E_g$) of 4.10 eV, with the valence band maximum (VBM) and the conduction band minimum (CBM) situated at 3.21 eV and −0.89 eV respectively. Theoretical simulations show that F-doping in the $Ta_2O_5$ crystal introduces the density of states near the Fermi level that cross the Fermi surface, yielding a metallic band structure (Fig. S15a–c†). However, this contradicts the experimental semiconductor band structure of s-$Ta_2O_5$ NRs (Fig. S14†), indicating that F does not contribute to the band structure of s-$Ta_2O_5$ NRs. Instead, applying a tensile strain along the [001] axis of the $Ta_2O_5$ crystal maintains the semiconductor band structure (Fig. S15d†), with only slight shifts in the band edges, consistent with experimental observations. This suggests that the subtle alterations in the band structure of s-$Ta_2O_5$ NRs are mainly attributed to strain effects rather than fluorine doping. These insights, along with the previous TEM, XAS, XPS, XRD, Raman, and EDS analyses, sufficiently verify that the crystal regions under tensile strain consist of pure $Ta_2O_5$, while fluorine is mainly located in the amorphous areas. Notably, the orthorhombic $Ta_2O_5$ crystal

structure is formed by corner-sharing or edge-sharing links between $TaO_6$ octahedra and $TaO_7$ polyhedra, featuring a distinctive interspace at the junction where a $TaO_6$ octahedron and a $TaO_7$ polyhedron share corners (Fig. S16†).[36] This interspace, characterized by a lower packing density of oxygen atoms, offers a potential site for F insertion. Given the smaller size and higher electronegativity of F atoms relative to oxygen, they readily occupy these interspaces and form Ta–F bonds, as confirmed by XAS and XPS analyses (Fig. 1e–h and S3†). The insertion of F into the $Ta_2O_5$ lattice would push away surrounding atoms, culminating in lattice expansion. This lattice expansion effect instigated by F insertion impacts neighboring $Ta_2O_5$ crystalline regions, engendering tensile strain. Consequently, the synthesized s-$Ta_2O_5$ NRs exhibit an ordered growth along the [001] direction, alternating between pure $Ta_2O_5$ crystalline regions and F-doped amorphous areas, containing tensile strain and associated cavities.

Notably, although $Ta_2O_5$ NRs maintain the same size and morphology as the s-$Ta_2O_5$ NRs after annealing at 750 °C (Fig. S6†), their XRD pattern and Raman spectrum (Fig. 1c and d) indicate that the tensile strain disappears. Furthermore, HRTEM images, captured with the electron beam directed along various axes of the $Ta_2O_5$ NR (Fig. S17†), display well-defined lattice fringes consistent with the orthorhombic $Ta_2O_5$ crystal structure. This is supported by the presence of sharp diffraction spots, free of the tail-dragging effect, in the corresponding FFT images, suggesting a well-crystallized single-crystal structure. GPA strain tensor mapping further verifies the absence of strain in the $Ta_2O_5$ NRs (Fig. S18†). After annealing, fluorine is eliminated (Fig. 1g and S3†), and the previously fluorine-doped $Ta_2O_5$ amorphous regions are converted into an ordered crystalline pure $Ta_2O_5$ phase (Fig. 1c, d, S3, S6, and S17†), resulting in the removal of tensile strain. Evidently, the creation of localized amorphous regions is the primary cause of the tensile strain in s-$Ta_2O_5$ NRs.

### Effect of tensile strain on $E_b$ in s-$Ta_2O_5$ NRs

To evaluate the effect of tensile strain on $E_b$, temperature-dependent photoluminescence (PL) spectroscopy was

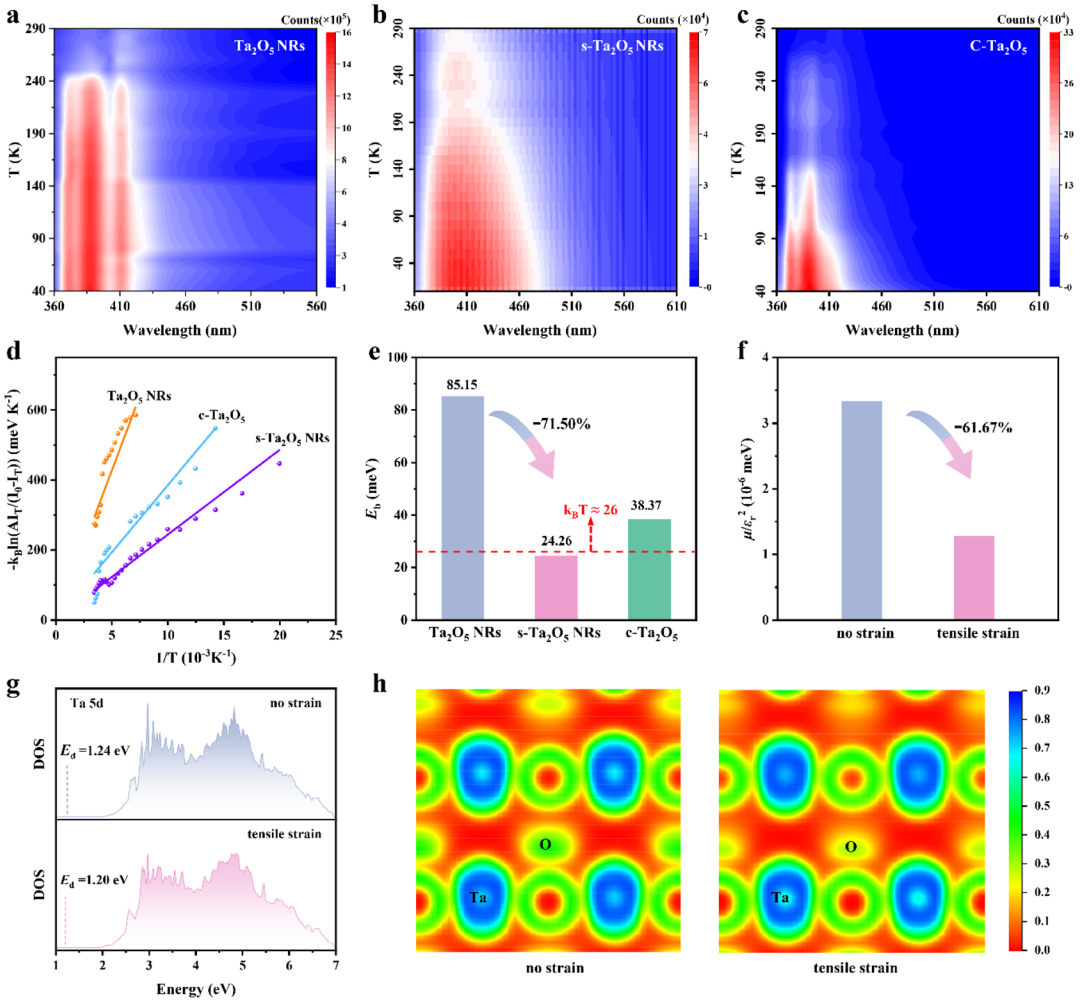


Fig. 3 The effect of tensile strain on the $E_b$ of s-$Ta_2O_5$ NRs. Temperature-dependent PL spectra of (a) $Ta_2O_5$ NRs, (b) s-$Ta_2O_5$ NRs and (c) c-$Ta_2O_5$. (d) Integrated PL emission intensity as a function of temperature. (e) Comparative $E_b$ values for s-$Ta_2O_5$ NRs, $Ta_2O_5$ NRs, and c-$Ta_2O_5$. (f) Calculated $\mu/\varepsilon_r^2$ values. (g) Ta 5d PDOS and corresponding d-band centers. (h) ELF plots for $Ta_2O_5$ without (left) and with (right) a tensile strain along [001].

meticulously performed. The PL spectra from all samples (Fig. 3a–c) exhibit a consistent increase in PL peak intensity as the temperature decreases, attributable to phonon-assisted relaxation. Accordingly, the $E_b$ values for various $Ta_2O_5$ samples were determined by employing the Arrhenius equation $I_T = I_0/(1 + A\exp(-E_b/k_BT))$ to fit the acquired PL data (Fig. 3d and S19†).[18] As stated within semiconductor physics, a reduction in size would weaken the dielectric screening effect, thereby increasing the exciton effect.[15,37,38] Indeed, $Ta_2O_5$ NRs exhibit a larger $E_b$ of 85.15 meV compared to c-$Ta_2O_5$, which has an $E_b$ of 38.37 meV (Fig. 3e).

However, introducing tensile strain results in a substantial decrease in the $E_b$ for s-$Ta_2O_5$ NRs (which have the same size and morphology as $Ta_2O_5$ NRs, Fig. S2 and S6†) to 24.26 meV, which is significantly lower than that of both the unstrained $Ta_2O_5$ NRs and c-$Ta_2O_5$ samples, and even below ambient thermal energy ($k_BT \approx 26$ meV), suggesting an easy dissociation of excitons into free charges during photocatalysis. According to the equation $E_b = \mu E_0/m_0\varepsilon_r^2$, $E_b$ is predominantly determined by the variables $\mu$ and $\varepsilon_r$.[39,40] To further examine the effect of strain on $E_b$, the $\mu$ and $\varepsilon_r$ values for $Ta_2O_5$ crystal models (Fig. S20†), both with and without a tensile strain along the [001] direction, were calculated (Fig. S21†). Fig. 3f illustrates that a tensile strain along the [001] direction markedly causes a 61.67% decrease in the value of $\mu/\varepsilon_r^2$, aligning well with the experimentally observed trends in $E_b$ variation. Both experimental and theoretical results robustly support the assertion that tensile strain can significantly lower the $E_b$ in $Ta_2O_5$ photocatalysts, which in turn weakens the coulombic interaction between photoexcited electrons and holes, enhancing charge separation efficiency, liberating more free charges, and promoting charge-driven photocatalytic reactions.

To explore the effect of tensile strain on $E_b$, we performed DFT calculations to assess the density of states (DOS) and electron localization function (ELF) in $Ta_2O_5$, both with and without the application of tensile strain. The d-band center theory offers an effective method for evaluating the bonding conditions in transition metals.[41–43] As illustrated in Fig. 3g, there is a discernible reduction in the partial density of states (PDOS) for Ta 5d above the Fermi level. Concurrently, there is a slight shift in the d-band center ($E_d$) from 1.24 eV to 1.20 eV. These observations, combined with the O 2p PDOS (Fig. S22†) suggest that tensile strain could weaken the antibonding interactions between Ta and O atoms, consequently decreasing the overlap between the Ta 5d and O 2p orbitals. The ELF offers an effective description of electron delocalization in solids,[44,45] serving as a valuable tool for the chemical bonds' classification.[46,47] Further scrutiny of the ELF contour plots on the (001) crystal plane (Fig. 3h and S23†) reveals a reduction in ELF values near oxygen atoms under a tensile strain along the [001] axis, indicating a lower charge density and increased electron delocalization in these areas. These observations collectively imply that tensile strain reduces the interaction between Ta 5d and O 2p orbitals, promoting a more delocalized pathway for efficient charge transport.[48] This, in turn, lessens the coulombic interaction between photoexcited electrons and holes in excitons, thereby lowering the $E_b$.

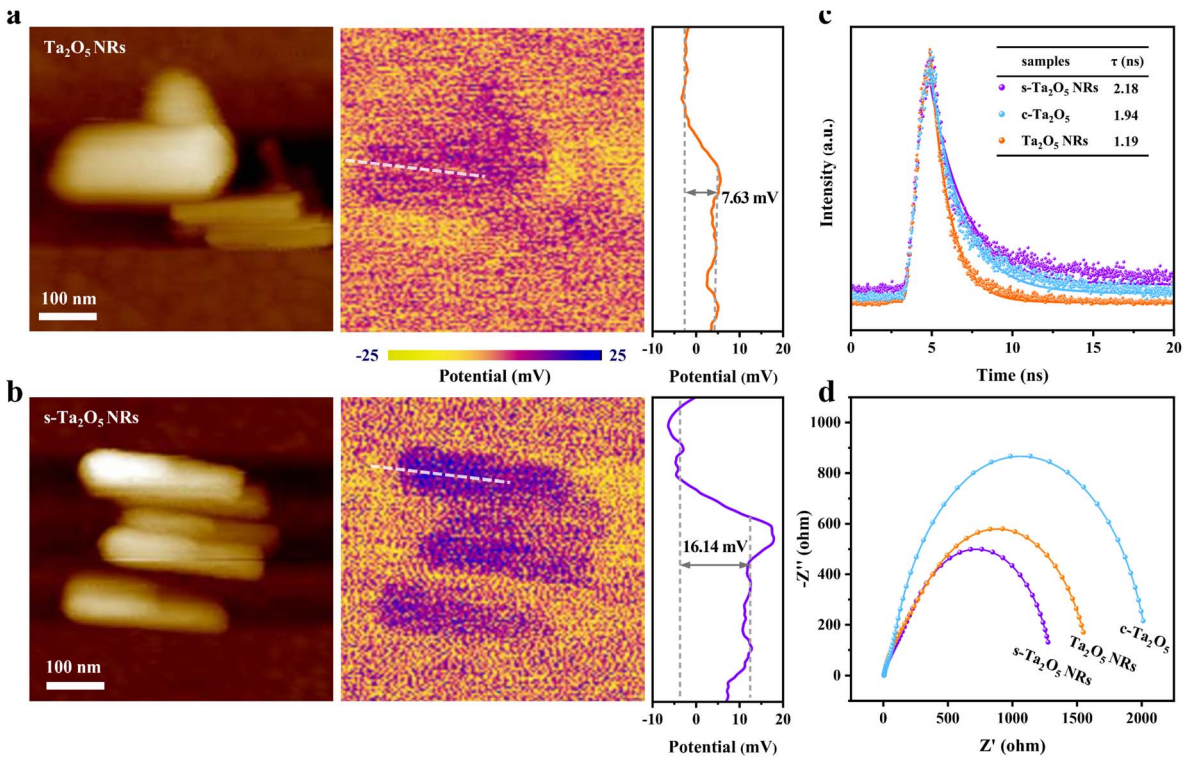


Fig. 4 The effect of tensile strain on charge transport in s-$Ta_2O_5$ NRs. Atomic force microscopy images (left) and the corresponding surface potentials measured with KPFM (right) of (a) $Ta_2O_5$ NRs and (b) s-$Ta_2O_5$ NRs. (c) Time-resolved transient PL decay. (d) EIS spectra.

### Effect of tensile strain on charge transport

Reducing $E_b$ facilitates the separation of photoexcited charge carriers, providing more free charge carriers for the photocatalytic reactions. To confirm this point, the influence of tensile strain on the charge transport was studied using Kelvin probe force microscopy (KPFM). Fig. 4a and b reveal that the surface potential of s-$Ta_2O_5$ NRs is considerably two times higher than that for unstrained $Ta_2O_5$ NRs, suggesting a lower work function and Fermi level, which are conducive to electron separation. Moreover, the influence of tensile strain on the lifetime of photo-generated charge carriers was further investigated using advanced time-resolved PL spectroscopy. In Fig. 4c, the PL lifetime of the s-$Ta_2O_5$ NRs reaches up to 2.18 ns, notably surpassing that for both $Ta_2O_5$ NRs (1.19 ns) and c-$Ta_2O_5$ (1.94 ns). This is indicative of the tensile strain's efficacy in diminishing electron–hole recombination rates within the s-$Ta_2O_5$ NRs, in line with the observed trend in the reduction of $E_b$. In parallel, electrochemical impedance spectra (EIS) provided additional evidence, where the s-$Ta_2O_5$ NRs exhibit the smallest semicircle in the Nyquist plots (Fig. 4d), signifying exceptional charge transfer capabilities and the most efficient charge migration when benchmarked against $Ta_2O_5$ NRs and c-$Ta_2O_5$. Collectively, these experimental results robustly validate that the introduction of tensile strain substantially diminishes exciton binding energy, thereby extending the lifetime of photo-generated charges and promoting effective charge separation and migration, which is highly beneficial for photogenerated charge-involved photocatalytic reactions.

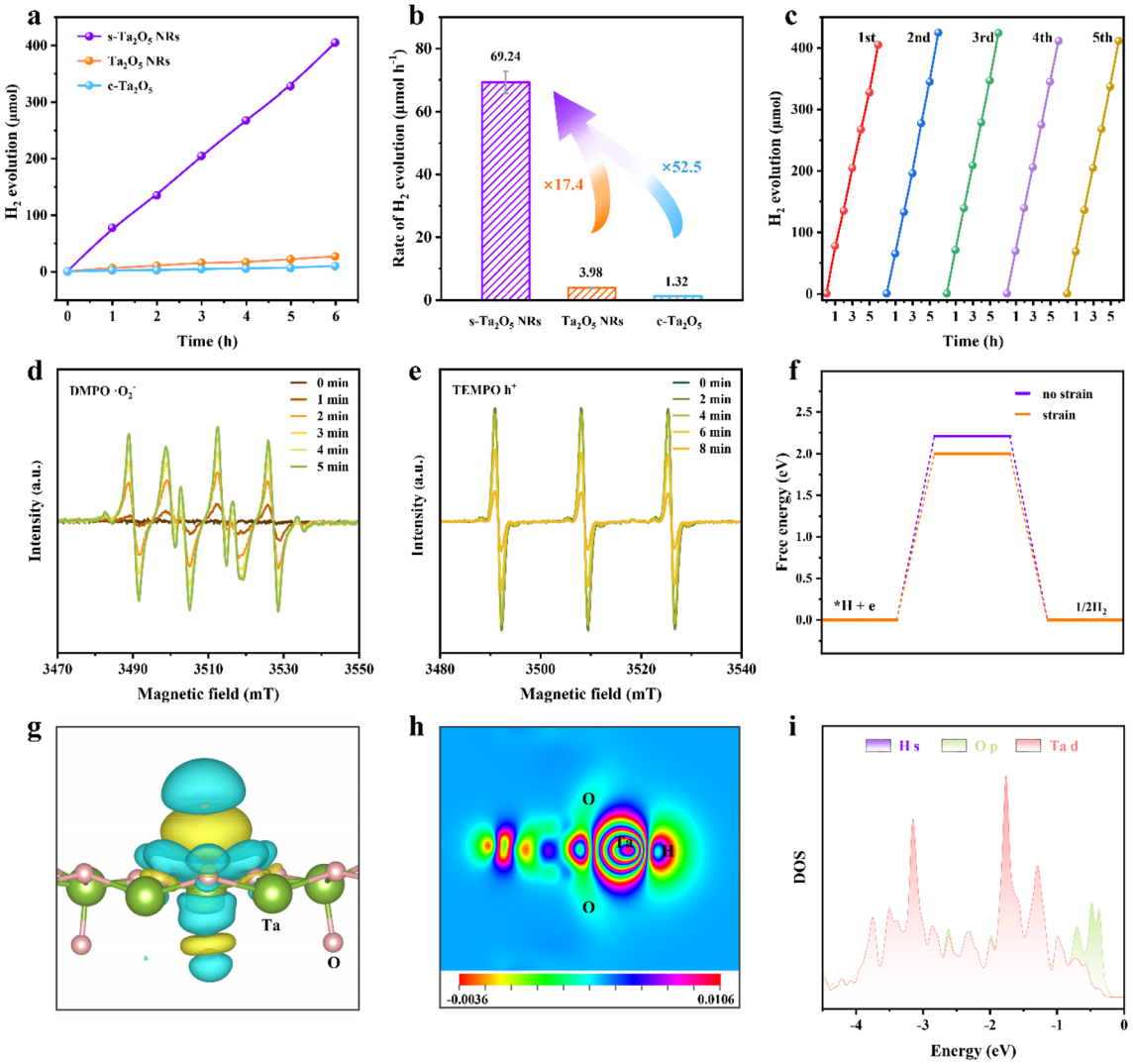


Fig. 5 Photocatalytic water splitting performances and mechanism of s-$Ta_2O_5$ NRs. (a) Photocatalytic $H_2$ production from water splitting for s-$Ta_2O_5$ NRs, $Ta_2O_5$ NRs, and c-$Ta_2O_5$ under UV light irradiation. (b) Comparative photocatalytic hydrogen evolution rates for s-$Ta_2O_5$ NRs, $Ta_2O_5$ NRs, and c-$Ta_2O_5$, respectively. (c) Repeated hydrogen generation performance of s-$Ta_2O_5$ NRs. *In situ* ESR spectra of (d) DMPO-trapped $^{\bullet}O_2^-$ radicals and (e) TEMPO-trapped $h^+$ in s-$Ta_2O_5$ NRs. (f) Gibbs free energy diagram for $H_2$ production through water splitting. (g) Charge density difference of H on $Ta_2O_5$ with a tensile strain along the [001] direction. The isosurface level is 0.00025 au. The yellow and blue shadows indicate charge accumulation and depletion, respectively. (h) Corresponding slice image of (g) across the (010) face. (i) PDOS of H 1s, Ta 5d, O 2p orbitals with H adsorbed on $Ta_2O_5$ with a tensile strain along the [001] direction.

**Photocatalytic activity**

To validate that tensile strain-induced decrease in $E_b$ can be leveraged to substantially promote charge separation, photocatalytic water splitting was further evaluated. Hydrogen production from photocatalytic water splitting using s-$Ta_2O_5$ NRs under ultraviolet illumination in a methanol/water solution was conducted and compared with that of $Ta_2O_5$ NRs and c-$Ta_2O_5$. Fig. 5a exhibits a direct proportional relationship between the duration of light illumination and the amount of hydrogen evolved, indicating a consistent photocatalytic activity over various $Ta_2O_5$ samples. Notably, s-$Ta_2O_5$ NRs achieve a hydrogen production rate of 69.24 μmol $h^{-1}$, significantly surpassing that of $Ta_2O_5$ NRs (3.98 μmol $h^{-1}$) and c-$Ta_2O_5$ (1.32 μmol $h^{-1}$), representing an increase by approximately 16.4 and 51.5 times, respectively (Fig. 5b). No hydrogen was detected in the absence of either irradiation or photocatalysts, suggesting $H_2$ production solely attributable to the photocatalytic reaction on the $Ta_2O_5$ catalysts. The s-$Ta_2O_5$ NRs demonstrate a steady linear rise in hydrogen production over five consecutive cycles (Fig. 5c), indicating robust catalytic activity and stability. Subsequent SEM and XRD analyses post-catalysis show no notable changes in the morphology or crystal structure (Fig. S24†), corroborating the structural integrity of s-$Ta_2O_5$ NRs throughout the photocatalytic reaction. The structural characterization above suggests that s-$Ta_2O_5$ NRs have comparable structure sizes (the specific surface areas of s-$Ta_2O_5$ NRs and $Ta_2O_5$ NRs were measured at approximately 15.8 and 11.9 $m^2$ $g^{-1}$ respectively) and nearly identical energy bands to $Ta_2O_5$ NRs. Moreover, no significant hydrogen was detected when both F-doped and undoped amorphous $Ta_2O_5$ samples were used as catalysts. Additionally, the F element is solely found in the amorphous region in s-$Ta_2O_5$ NRs; these areas will not be involved in photo-excitation and production of photogenerated charges. Taken together, these results emphatically validate that the resultant tensile strain in s-$Ta_2O_5$ NRs effectively decreases exciton binding energy, thereby enhancing charge separation and ultimately leading to an exceptional enhancement of photocatalytic activity.

To delve into the underlying photocatalytic mechanisms, *in situ* ESR spectroscopy was employed to monitor the reactive species throughout the photocatalytic process. 2,2,6,6-Tetramethyl-1-piperidinyloxy (TEMPO) and 5,5-dimethyl-1-pyrroline-*N*-oxide (DMPO) radicals as scavengers were utilized for the direct observation of photogenerated holes and superoxide radicals ($^{\cdot}O_2^-$) respectively. The DMPO signal, absent under dark conditions, markedly increases with light exposure and continues to rise over time (Fig. 5d), indicating a steady production of photogenerated electrons. This is further corroborated by the detection of photogenerated $^{\cdot}OH$ (Fig. S25†). In contrast, the TEMPO signal diminishes when exposed to light and further decreases with prolonged illumination (Fig. 5e), suggesting the sustained formation and accumulation of photogenerated holes. Further, DFT calculations reveal that the tensile strain can lower the Gibbs free energy for hydrogen production, thereby lowering the energy barrier for both water molecule adsorption and hydrogen gas release (Fig. 5f), facilitating the water-splitting reaction. Charge density difference calculation shows a reduced charge on Ta atoms and a heightened charge around H atoms, indicating a direct electron transfer from Ta to H atoms (Fig. 5g and h). PDOS analysis further confirmed a robust interaction between Ta 5d and H 1s orbitals (Fig. 5i). Integrating ESR analyses with DFT calculations, it is inferred that the introduction of tensile strain significantly lowers $E_b$, endows a strong interaction between Ta 5d and H 1s orbitals, and reduces the Gibbs free energy of hydrogen production, thereby facilitating efficient electron transfer for water reduction and hydrogen generation, as well as sustaining photogenerated holes for the photocatalytic oxidation reactions.

## Conclusions

In summary, we have successfully fabricated s-$Ta_2O_5$ single crystal nanorods with tensile strain by ingeniously engineering a crystalline/amorphous interface within them through the strategic insertion of F atoms into the interspaces shared by the vertices of $TaO_6$ octahedra and $TaO_7$ polyhedra. This strain weakens the interaction between Ta 5d and O 2p orbitals in s-$Ta_2O_5$ NRs, thereby reducing charge localization and building a more delocalized charge transport channel. This significantly decreases the $E_b$ to below ambient thermal energy (~26 meV), marking a 71.50% decrease compared to their unstrained counterparts. A lower $E_b$ contributes to enhanced carrier lifetime and surface potential, improved charge separation efficiency, and a lowered hydrogen evolution reaction barrier, thereby endowing direct electron transfer from Ta atoms to protons. As a result, the s-$Ta_2O_5$ NRs exhibit a markedly improved photocatalytic hydrogen production activity, with generation rates surpassing those of $Ta_2O_5$ NRs and c-$Ta_2O_5$ by 16.4 and 51.5 times, respectively. The study not only offers an effective strategy to reduce exciton binding energy through strain-induced charge delocalization, but also paves a novel avenue for the design of highly efficient photoconversion systems.

## Data availability

All experimental procedures, computational sections, and associated data are included in the article and ESI.†

## Author contributions

J. D., Y. L., and T. Z. conceived and directed the project. J. D. designed and executed the experiments. J. D. and Y. L. co-wrote the paper. J. D., Y. W., Y. Z., and Y. L. performed and analyzed the DFT calculations. J. D. and Y. L. conducted and interpreted the XAFS spectroscopy. J. D. and C. L. collaboratively conducted PL. J. D., J. H., and Y. Z. jointly performed AFM and KPFM. J. D. and D. Z. carried out and discussed the GPA. J. D., Y. L., X. J., J. G., and T. Z. revised the paper. J. C. participated in the discussion of the catalytic mechanism. All authors discussed the results and contributed to the manuscript preparation.

## Conflicts of interest

The authors declare no competing financial interest.

## Acknowledgements

This work was financially supported by the National Natural Science Foundation of China (22071069, 22173048, and 22103026), the Project Funded by the China Postdoctoral Science Foundation (2019M662604), and the Scientific Research Fund Project of Wuhan Institute of Technology (no. 23QD06). We thank the Analytical and Testing Center at Huazhong University of Science and Technology for their technical support, especially Dr Jianquan Zhao. We also acknowledge the support of the HPC platform at HUST. Furthermore, the authors greatly appreciate the beam time allocation and assistance provided by beamline BL11B at the Shanghai Synchrotron Radiation Facility.

## References

1 T. Hisatomi and K. Domen, *Nat. Catal.*, 2019, **2**, 387–399.
2 W. H. Lee, C. W. Lee, G. D. Cha, B.-H. Lee, J. H. Jeong, H. Park, J. Heo, M. S. Bootharaju, S.-H. Sunwoo, J. H. Kim, K. H. Ahn, D.-H. Kim and T. Hyeon, *Nat. Nanotechnol.*, 2023, **18**, 754–762.
3 X. P. Tao, Y. Zhao, S. Y. Wang, C. Li and R. G. Li, *Chem. Soc. Rev.*, 2022, **51**, 3561–3608.
4 J. Y. Y. Loh, N. P. Kherani and G. A. Ozin, *Nat. Sustainability*, 2021, **4**, 466–473.
5 S. P. Che, J. H. Zhang, F. Z. Mou, X. Guo, J. E. Kauffman, A. Sen and J. G. Guan, *Research*, 2022, **2022**, 9816562.
6 M. Z. Li, J. Z. Wang, Q. Y. Wang, H. L. Lu, G. F. Wang and H. G. Fu, *Chem. Sci.*, 2024, **15**, 1860–1869.
7 P. Zhou, I. A. Navid, Y. Ma, Y. Xiao, P. Wang, Z. Ye, B. Zhou, K. Sun and Z. Mi, *Nature*, 2023, **613**, 66–70.
8 J. Y. Duan, G. Y. Mou, S. Zhang, S. Wang and J. G. Guan, *J. Mater. Chem. A*, 2015, **3**, 14686–14695.
9 Q. Wang, C. Pornrungroj, S. Linley and E. Reisner, *Nat. Energy*, 2022, **7**, 13–24.
10 B. Jin, N. Zuo, Z. Y. Hu, W. J. Cui, R. Y. Wang, G. Van Tendeloo, X. Zhou and T. Y. Zhai, *Adv. Funct. Mater.*, 2020, **30**, 2006166.
11 H. Wang, W. X. Liu, X. He, P. Zhang, X. D. Zhang and Y. Xie, *J. Am. Chem. Soc.*, 2020, **142**, 14007–14022.
12 S. Kang, K. Kim, B. H. Kim, J. Kim, K. I. Sim, J. U. Lee, S. Lee, K. Park, S. Yun, T. Kim, A. Nag, A. Walters, M. Garcia-Fernandez, J. Li, L. Chapon, K. J. Zhou, Y. W. Son, J. H. Kim, H. Cheong and J. G. Park, *Nature*, 2020, **583**, 785–789.
13 Q. C. Burlingame, X. Liu, M. L. Ball, B. P. Rand and Y. L. Loo, *Energy Environ. Sci.*, 2023, **16**, 1742–1751.
14 J. Pradhan, A. Das, K. Kundu, Chahat and K. Biswas, *Chem. Sci.*, 2022, **13**, 9952–9959.
15 P. Chen, T. L. Atallah, Z. Y. Lin, P. Q. Wang, S. J. Lee, J. Q. Xu, Z. H. Huang, X. D. Duan, Y. Ping, Y. Huang, J. R. Caram and X. F. Duan, *Nature*, 2021, **599**, 404–410.
16 Y. Qian, Y. Han, X. Zhang, G. Yang, G. Zhang and H.-L. Jiang, *Nat. Commun.*, 2023, **14**, 3083.
17 C. Li, J. Liu, H. Li, K. Wu, J. Wang and Q. Yang, *Nat. Commun.*, 2022, **13**, 2357.
18 Z.-A. Lan, G. Zhang, X. Chen, Y. Zhang, K. A. I. Zhang and X. Wang, *Angew. Chem., Int. Ed.*, 2019, **58**, 10236–10240.
19 M. B. Price, P. A. Hume, A. Ilina, I. Wagner, R. R. Tamming, K. E. Thorn, W. T. Jiao, A. Goldingay, P. J. Conaghan, G. Lakhwani, N. Davis, Y. F. Wang, P. Y. Xue, H. Lu, K. Chen, X. W. Zhan and J. M. Hodgkiss, *Nat. Commun.*, 2022, **13**, 2827.
20 M. H. Huang, S. Mao, H. Feick, H. Q. Yan, Y. Y. Wu, H. Kind, E. Weber, R. Russo and P. D. Yang, *Science*, 2001, **292**, 1897–1899.
21 A. Raja, L. Waldecker, J. Zipfel, Y. Cho, S. Brem, J. D. Ziegler, M. Kulig, T. Taniguchi, K. Watanabe, E. Malic, T. F. Heinz, T. C. Berkelbach and A. Chernikov, *Nat. Nanotechnol.*, 2019, **14**, 832–837.
22 Y. Lei, Y. Li, C. Lu, Q. Yan, Y. Wu, F. Babbe, H. Gong, S. Zhang, J. Zhou, R. Wang, R. Zhang, Y. Chen, H. Tsai, Y. Gu, H. Hu, Y.-H. Lo, W. Nie, T. Lee, J. Luo, K. Yang, K.-I. Jang and S. Xu, *Nature*, 2022, **608**, 317–323.
23 A. Raja, A. Chaves, J. Yu, G. Arefe, H. M. Hill, A. F. Rigosi, T. C. Berkelbach, P. Nagler, C. Schueller, T. Korn, C. Nuckolls, J. Hone, L. E. Brus, T. F. Heinz, D. R. Reichman and A. Chernikov, *Nat. Commun.*, 2017, **8**, 15251.
24 Y. B. Shi, J. Li, C. L. Mao, S. Liu, X. B. Wang, X. F. Liu, S. X. Zhao, X. Liu, Y. Q. Huang and L. Z. Zhang, *Nat. Commun.*, 2021, **12**, 5923.
25 N. Kornienko, J. Z. Zhang, K. K. Sakimoto, P. D. Yang and E. Reisner, *Nat. Nanotechnol.*, 2018, **13**, 890–899.
26 B. Wu, J. Z. Fan, J. Y. Han, Y. Su, M. P. Zhuo, J. H. Sun, Y. Gao, S. Chen, J. J. Wu, Z. S. Wang and X. D. Wang, *Adv. Mater.*, 2023, **35**, 2206272.
27 J. Kosco, S. Gonzalez-Carrero, C. T. Howells, T. Fei, Y. F. Dong, R. Sougrat, G. T. Harrison, Y. Firdaus, R. Sheelamanthula, B. Purushothaman, F. Moruzzi, W. D. Xu, L. Y. Zhao, A. Basu, S. De Wolf, T. D. Anthopoulos, J. R. Durrant and I. McCulloch, *Nat. Energy*, 2022, **7**, 340–351.
28 A. Ciarrocchi, F. Tagarelli, A. Avsar and A. Kis, *Nat. Rev. Mater.*, 2022, **7**, 449–464.
29 S. Nishioka, K. Hojo, L. Xiao, T. Gao, Y. Miseki, S. Yasuda, T. Yokoi, K. Sayama, T. E. Mallouk and K. Maeda, *Sci. Adv.*, 2022, **8**, eadc9115.
30 J. V. Passarelli, C. M. Mauck, S. W. Winslow, C. F. Perkinson, J. C. Bard, H. Sai, K. W. Williams, A. Narayanan, D. J. Fairfield, M. P. Hendricks, W. A. Tisdale and S. I. Stupp, *Nat. Chem.*, 2020, **12**, 672–682.
31 F. Li, Z. H. Fang, Z. H. Xu and Q. J. Xiang, *Energy Environ. Sci.*, 2024, **17**, 497–509.
32 V. Gurylev, *Mater. Today Sustainability*, 2022, **18**, 100131.
33 P. Zhang, J. J. Zhang and J. L. Gong, *Chem. Soc. Rev.*, 2014, **43**, 4395–4422.

34 Z. Wang, Y. Inoue, T. Hisatomi, R. Ishikawa, Q. Wang, T. Takata, S. Chen, N. Shibata, Y. Ikuhara and K. Domen, *Nat. Catal.*, 2018, **1**, 756–763.
35 M. A. Lange, I. Khan, P. Opitz, J. Hartmann, M. Ashraf, A. Qurashi, L. Praedel, M. Panthoefer, A. Cossmer, J. Pfeifer, F. Simon, M. von der Au, B. Meermann, M. Mondeshki, M. N. Tahir and W. Tremel, *Adv. Mater.*, 2021, **33**, 2007434.
36 Y. Yang and Y. Kawazoe, *Phys. Rev. Mater.*, 2018, **2**, 034602.
37 Y. Zhang, F. K. Wang, X. Feng, Z. Zhang, K. L. Liu, F. F. Xia, W. X. Liang, X. Z. Hu, Y. Ma, H. Q. Li, G. C. Xing and T. Y. Zhai, *Adv. Funct. Mater.*, 2022, **32**, 2205757.
38 L. K. Li, J. Kim, C. H. Jin, G. J. Ye, D. Y. Qiu, F. H. da Jornada, Z. W. Shi, L. Chen, Z. C. Zhang, F. Y. Yang, K. Watanabe, T. Taniguchi, W. Ren, S. G. Louie, X. H. Chen, Y. B. Zhang and F. Wang, *Nat. Nanotechnol.*, 2017, **12**, 21–25.
39 M. Baranowski and P. Plochocka, *Adv. Energy Mater.*, 2020, **10**, 1903659.
40 A. Miyata, A. Mitioglu, P. Plochocka, O. Portugall, J. T. W. Wang, S. D. Stranks, H. J. Snaith and R. J. Nicholas, *Nat. Phys.*, 2015, **11**, 582–587.
41 N. Hong Nhan, T. Reier, H.-S. Oh, M. Gliech, P. Paciok, V. Thu Ha Thi, D. Teschner, M. Heggen, V. Petkov, R. Schloegl, T. Jones and P. Strasser, *Nat. Catal.*, 2018, **1**, 841–851.
42 K. Jia, J. Ma, J. Wang, Z. Liang, G. Ji, Z. Piao, R. Gao, Y. Zhu, Z. Zhuang, G. Zhou and H.-M. Cheng, *Adv. Mater.*, 2023, **35**, 2208034.
43 H. Yang, C. L. Dong, H. M. Wang, R. J. Qi, L. Q. Gong, Y. R. Lu, C. H. He, S. H. Chen, B. You, H. F. Liu, J. L. Yao, X. L. Jiang, X. P. Guo and B. Y. Xia, *Proc. Natl. Acad. Sci. U. S. A.*, 2022, **119**, e2202812119.
44 A. Savin, R. Nesper, S. Wengert and T. F. Fassler, *Angew. Chem., Int. Ed.*, 1997, **36**, 1809–1832.
45 X. Feng, K. J. Bu, T. Liu, S. H. Guo, Z. D. Sun, T. H. Fu, Y. S. Xu, K. L. Liu, S. J. Yang, Y. H. Zhao, H. Q. Li, X. J. Lu and T. Y. Zhai, *Angew. Chem., Int. Ed.*, 2022, **62**, e202217238.
46 D. B. Chesnut and A. Savin, *J. Am. Chem. Soc.*, 1999, **121**, 2335–2336.
47 B. Silvi and A. Savin, *Nature*, 1994, **371**, 683–686.
48 J. Y. Duan, T. Y. Liu, Y. H. Zhao, R. O. Yang, Y. Zhao, W. B. Wang, Y. W. Liu, H. Q. Li, Y. F. Li and T. Y. Zhai, *Nat. Commun.*, 2022, **13**, 2039.